

# eKalibr: Dynamic Intrinsic Calibration for Event Cameras From First Principles of Events

Shuolong Chen<sup>1</sup>, Xingxing Li<sup>1</sup>, Liu Yuan<sup>1</sup>, and Ziao Liu<sup>1</sup>

**Abstract**—The bio-inspired event camera has garnered extensive research attention in recent years, owing to its significant potential derived from its high dynamic range and low latency characteristics. Similar to the standard camera, the event camera requires precise intrinsic calibration to facilitate further high-level visual applications, such as pose estimation and mapping. While several calibration methods for event cameras have been proposed, most of them are either (i) engineering-driven, heavily relying on conventional image-based calibration pipelines, or (ii) inconvenient, requiring complex instrumentation. To this end, we propose an accurate and convenient intrinsic calibration method for event cameras, named *eKalibr*, which builds upon a carefully designed event-based circle grid pattern recognition algorithm. To extract target patterns from events, we perform event-based normal flow estimation to identify potential events generated by circle edges, and cluster them spatially. Subsequently, event clusters associated with the same grid circles are matched and grouped using normal flows, for subsequent time-varying ellipse estimation. Fitted ellipse centers are time-synchronized, for final grid pattern recognition. We conducted extensive experiments to evaluate the performance of *eKalibr* in terms of pattern extraction and intrinsic calibration. The implementation of *eKalibr* is open-sourced at (<https://github.com/Unsigned-Long/eKalibr>) to benefit the research community.

**Index Terms**—Event camera, intrinsic calibration, event-based normal flow, circle grid pattern recognition

## I. INTRODUCTION AND RELATED WORKS

THE event camera, as a bio-inspired novel vision sensor, could overcome the challenges of motion blur and low-illumination degradation encountered by the conventional camera, owing to its low latency and high dynamic range [1], [2]. To facilitate further event-based applications, accurate intrinsic calibration is generally required for event cameras. Although some event cameras, such as *DAVIS* series [3] and *CeleX* series [4], are capable of standard image output, thereby enabling conventional frame-based intrinsic calibration [5], others, such as *DVS-Gen* series [6], only support event output, leaving their intrinsic calibration an open question.

The reason is straightforward. In visual intrinsic calibration, artificial targets, e.g., April Tags [7] and checkerboards [8], are commonly employed for accurate intrinsic determination. For conventional cameras, precise image-based target pattern recognition has been extensively studied and solved [8], [9].

This work was supported by the the National Science Fund for Distinguished Young Scholars of China under Grant 42425401.

The authors are with the School of Geodesy and Geomatics (SGG), Wuhan University (WHU), Wuhan 430070, China. Corresponding author: Xingxing Li (xxli@sgg.whu.edu.cn). The specific contributions of the authors to this work are listed in Section **CRedit Authorship Contribution Statement** at the end of the article.

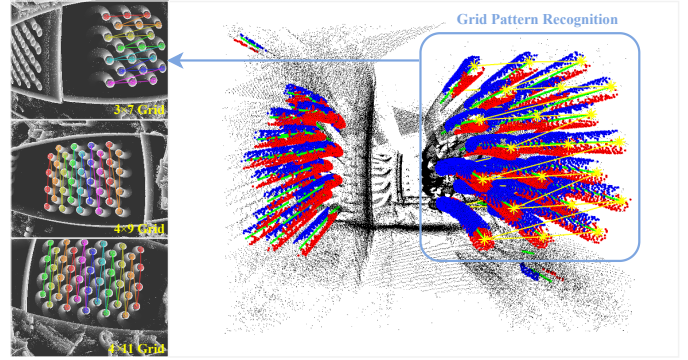


Fig. 1. The runtime visualization of circle grid pattern recognition in *eKalibr*. *eKalibr* extracts patterns from raw events in spatiotemporal domain from first principles of events.

However, for event cameras, due to their asynchronous spatiotemporal output, image-based pattern recognition methods are not directly applicable, making extracting accurate target patterns from raw event streams a challenge (has yet to be effectively resolved). Given that the visual intrinsic estimation (i.e., determining intrinsics from 2D-3D correspondences) is fundamentally the same for vision sensors, and has been well-resolved [10], the key issue in event camera calibration lies in accurately identifying target patterns from raw events.

The most straightforward approach to recognizing reliable and accurate target patterns from event streams is to modify the conventional artificial targets to accommodate event cameras, which is exactly the method used in [11] and [12]. Given the fact that event camera generates events by detecting brightness changes, the authors of [11] and [12] employed a blinking light emitting diode (LED) grid board flashing at a fixed frequency to trigger the event camera, generating low-noise accumulation event images for grid pattern extraction. Similarly, leveraging LEDs but extracting the target patterns in the phase domain rather than the spatial (intensity) domain, Cai et al. [13] propose a Fourier-transform-based calibration method, which significantly mitigates the impact of event noise during calibration. Using LEDs for pattern extraction is grounded in first principles of events, easy to understand, and generally yields accurate calibration results. However, several inherent limitations exist in this approach: (i) it imposes high requirements on the hardware (calibration target), and (ii) a more **critical** one is that it's a static calibration method, which cannot be used for subsequent multi-camera or event-inertial spatiotemporal calibration that requires motion excitation [14].

Another approach for target pattern recognition for event cameras is to directly construct image frames from events and subsequently apply the well-established frame-based calibra-

tion methods for intrinsic determination, which is also intuitively understandable and could overcome limitations of LED-based methods. Gehrig et al. [15] and Muglikar et al. [16] are the first to apply event-to-image frameworks for event camera calibration. Their approach leverages images constructed by *E2VID* [17] to perform frame-based intrinsic calibration within the *Kalibr* [5]. Although the impressive performance of event-to-image reconstruction frameworks such as *E2VID* [17] and *EVSNN* [18] should be acknowledged, the accuracy of their reconstructed images remains inadequate for precise calibration. Furthermore, these frameworks are susceptible to noise, resulting in low repeatability and reliability of calibration.

An alternative approach is to directly extract target patterns from raw events for calibration, which is the most rooted in first principles of events, yet is also highly challenging due to the asynchrony, noise, and spatial sparsity of the events [1]. Huang et al. [19] are the first to focus on recognizing target patterns from events generated by relative motion between the camera and artificial target. They cluster events generated by a circle grid board using density-based spatial clustering (DBSCAN) for pattern recognition. Similarly, leveraging DBSCAN, Salah et al. [20] propose an efficient reweighted least squares (eRWLS) method to determine event cylinder centers associated with grid circles. Both [19] and [20] directly cluster accumulated events, making them sensitive to noise and generally resulting in a large number of outlier candidate clusters for grid circles. Considering this, Wang et al. [21] designed a novel circle grid board with cross points for efficient pattern recognition and subsequent joint event-frame spatiotemporal calibration. A carefully designed event-oriented noise suppression pipeline is also presented in [21]. However, introducing additional cross points in the circle grid board could give rise to potential noise events, thereby negatively affecting circle center determination through cylinder fitting.

Considering the issues present in the aforementioned methods, grounded in first principles of events, we propose a rigorous, accurate, and event-based target pattern recognition method oriented to conventional circle grid boards, for precise intrinsic calibration of event cameras, named *eKalibr* (see Fig. 1). We first perform event-based normal flow estimation to identify inlier events, and then spatially and homopolarly cluster them by contour searching. Event clusters would be matched based on the prior knowledge from circle-oriented normal flow distribution. Finally, time-varying ellipses would be estimated using raw events within each event cluster, for synchronous grid pattern extraction from ellipse centers. *eKalibr* makes the following (potential) contributions:

- 1) We propose a dynamic intrinsic calibration method for event cameras from the first principles of events, which leverages the **common** circle grid board, thus offering both convenience and extensibility.
- 2) A rigorous and accurate event-based pattern recognition approach oriented to the circle grid board is designed to identify grid patterns from raw events for intrinsic estimation. This approach has the **potential** to extend to other event-related calibration, such as event-inertial spatiotemporal calibration.
- 3) Sufficient experiments were conducted to evaluate the

proposed *eKalibr*. Both datasets and code implementations are open-sourced, to benefit the robotic community if possible.

## II. PRELIMINARIES

This section provides necessary notations and definitions used throughout the article. The camera intrinsic model and normal flow involved in this work are also introduced, ensuring a self-contained presentation for the reader.

### A. Notations and Definitions

The event camera detects brightness change and generates events at pixels where the intensity difference exceeds the contrast sensitivity [2]. We denote the  $j$ -th generated event as  $e_j$  in this article, which is defined as:

$$e_j \triangleq \{\tau_j, \mathbf{x}_j, p_j\} \quad \text{s.t.} \quad \mathbf{x}_j = [x_j, y_j]^\top \in \mathbb{Z}^2, p_j \in \{-1, +1\} \quad (1)$$

where  $\tau_j$  is the time of event  $e_j$  stamped by the camera;  $\mathbf{x}_j$  denotes the two-dimensional (2D) pixel coordinates where the event locates;  $p_j$  is the polarity of the event, indicating the direction of brightness change. In terms of coordinate systems, we use  $\underline{\mathcal{F}}_w$  and  $\underline{\mathcal{F}}_c$  to represent the world frame (i.e., the coordinate system of the circle grid pattern) and camera frame, respectively. The three-dimensional (3D) rigid-body transformation from  $\underline{\mathcal{F}}_w$  to  $\underline{\mathcal{F}}_c$  is parameterized as the Euclidean matrix:

$$\mathbf{T}_w \triangleq \begin{bmatrix} \mathbf{R}_w^c & \mathbf{p}_w^c \\ \mathbf{0}_{1 \times 3} & 1 \end{bmatrix} \in \text{SE}(3) \quad (2)$$

where  $\mathbf{R}_w^c \in \text{SO}(3)$  and  $\mathbf{p}_w^c \in \mathbb{R}^3$  denote the rotation matrix and translation vector, respectively. Finally, we represent the noisy measurements and estimated quantities by  $(\cdot)$  and  $(\hat{\cdot})$  respectively, mainly appearing in least-squares problem representation.

### B. Camera Intrinsic Model

The camera intrinsic model consists of the projection model and the distortion model, defining the correspondence between 3D objects in the world frame and 2D pixels in the image plane. Various projection and distortion models exist, such as pinhole [22] and double sphere [23] projection models, as well as radial-tangential [24] and equidistant (Fisheye) [25] distortion models. In this work, the pinhole projection model and radial-tangential distortion model are considered, and the corresponding camera model can be described as follows:

$$\mathbf{x}_p = \pi(\mathbf{P}^c, \mathbf{x}_{\text{intr}}) \triangleq \begin{bmatrix} f_x & 0 & c_x \\ 0 & f_y & c_y \end{bmatrix} \cdot \begin{bmatrix} x'' \\ y'' \\ 1 \end{bmatrix} \quad (3)$$

with

$$\begin{aligned} \mathbf{x}_{\text{intr}} &\triangleq \mathbf{x}_{\text{proj}} \cup \mathbf{x}_{\text{dist}} \\ \mathbf{x}_{\text{proj}} &\triangleq \{f_x, f_y, c_x, c_y\}, \quad \mathbf{x}_{\text{dist}} \triangleq \{k_1, k_2, p_1, p_2\} \end{aligned} \quad (4)$$

and

$$\begin{aligned} x'' &= x' \cdot (1 + k_1 \cdot r^2 + k_2 \cdot r^4) + 2p_1 \cdot x' \cdot y' + p_2 \cdot (r^2 + 2x'^2) \\ y'' &= y' \cdot (1 + k_1 \cdot r^2 + k_2 \cdot r^4) + 2p_2 \cdot x' \cdot y' + p_1 \cdot (r^2 + 2y'^2) \end{aligned} \quad (5)$$

$$x' = \mathbf{p}^c(x)/\mathbf{p}^c(z), \quad y' = \mathbf{p}^c(y)/\mathbf{p}^c(z), \quad r^2 = x'^2 + y'^2$$

where  $\pi(\cdot)$  represents the camera projection function projecting a 3D point  $\mathbf{p}^c$  in  $\underline{\mathcal{F}}_c$  onto the 2D image plane as  $\mathbf{x}_p$ ;  $\mathbf{x}_{\text{intr}}$  denotes the camera intrinsics, including projection coefficients

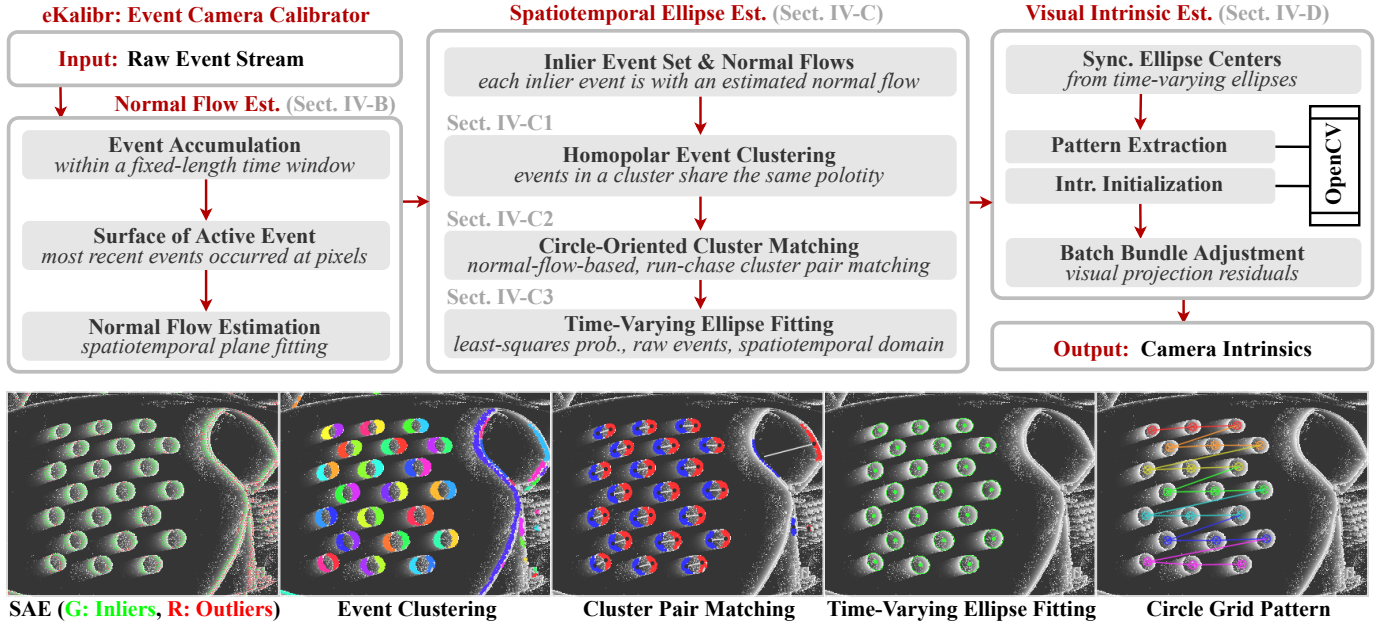


Fig. 2. Illustration of the pipeline of the proposed event-based visual intrinsic calibration method. A detailed description of the pipeline is provided in Section III-A, while detailed methodology is presented in Section III-B, Section III-C, and Section III-D.

$\mathbf{x}_{\text{proj}}$  and distortion coefficients  $\mathbf{x}_{\text{dist}}$ ;  $f_{x|y}$  and  $c_{x|y}$  denote the focal lengths and principal point respectively, while  $k_{1|2}$  and  $p_{1|2}$  are radial and tangential distortion coefficients. The purpose of camera (intrinsic) calibration is to determine  $\mathbf{x}_{\text{intr}}$ .

### C. Normal Flow

Events are mostly generated by moving high-gradient regions (e.g., edges) in the image [26], and are thus naturally associated with the image gradient. In the standard vision, the first-order Horn-Schunck model [27] gives the following constraint (higher-order items are not considered here):

$$\mathcal{I}(\mathbf{x} + \delta\mathbf{x}, \tau + \delta\tau) \approx \mathcal{I}(\mathbf{x}, \tau) + \nabla_{\mathbf{x}}\mathcal{I} \cdot \delta\mathbf{x} + \nabla_{\tau}\mathcal{I} \cdot \delta\tau \quad (6)$$

where  $\mathcal{I}(\mathbf{x}, \tau)$  denotes the image intensity at position  $\mathbf{x}$  and time  $\tau$ ;  $\nabla_{\mathbf{x}}\mathcal{I}$  and  $\nabla_{\tau}\mathcal{I}$  are spatial and temporal image gradient, respectively. Under the assumption of constant image intensity, by dividing (6) by  $\delta\tau$ , we obtain:

$$\nabla_{\mathbf{x}}\mathcal{I} \cdot \mathbf{v} = -\nabla_{\tau}\mathcal{I} \quad \text{s.t.} \quad \mathbf{v} \triangleq \frac{d\mathbf{x}}{d\tau} = \lim_{\delta\tau \rightarrow 0} \frac{\delta\mathbf{x}}{\delta\tau} \quad (7)$$

where  $\mathbf{v}$  is exactly the well-known optical flow (motion flow). Subsequently, by projecting the optical flow onto the image gradient direction  $\nabla_{\mathbf{x}}\mathcal{I}$  and introducing (7), we can derive the normal flow  $\mathbf{n}$  as follows:

$$\mathbf{n} \triangleq \frac{\nabla_{\mathbf{x}}\mathcal{I} \cdot \mathbf{v}}{\|\nabla_{\mathbf{x}}\mathcal{I}\|} \cdot \frac{\nabla_{\mathbf{x}}\mathcal{I}}{\|\nabla_{\mathbf{x}}\mathcal{I}\|} = -\frac{\nabla_{\tau}\mathcal{I}}{\|\nabla_{\mathbf{x}}\mathcal{I}\|^2} \cdot \nabla_{\mathbf{x}}\mathcal{I}. \quad (8)$$

The normal flow  $\mathbf{n}$  can be directly computed from raw event stream by fitting spatiotemporal planes (see Section III-B), facilitating subsequent circle grid extraction and calibration.

## III. METHODOLOGY

This section presents the detailed pipeline of the proposed event-based visual intrinsic calibration method.

### A. Overview

1) *Pipeline Description*: The general pipeline of the proposed method is shown in Fig. 2. Given raw event stream,

we first construct surface of active event (SAE) [28] within a fixed-length time window, and subsequently estimate normal flows of active events, see Section III-B. The inlier events in normal flow estimation would be homopolarly clustered (see Section III-C1), and then one-to-one matched to identify cluster pairs that are generated by the same circle in the grid pattern (see Section III-C2). For each cluster pair, we fit time-varying ellipses to determine the time-continuous curve of the centers of potential grid circles (see Section III-C3). Subsequently, time-varying centers would be sampled temporally to the end time of the window to obtain synchronized centers for grid extraction. Finally, based on extracted circle grid patterns, camera intrinsics can be determined, see Section III-D.

2) *Motivation Behind the Pipeline*: To enhance readers' understanding, we would like to be emboldened to provide our insights into the designed pipeline that is shown in Fig. 2. We employ the circle grid pattern in this work due to its simplicity and motion invariance for events (detailed in [20]). To accurately extract the circle grid pattern from raw events in the spatiotemporal domain, our motivation is to first identify raw events generated by the edges of each grid circle, and then determine centers of grid circles using associated raw events. To achieve this, we adopt the normal flow estimation, which could provide (i) inlier events for clustering and (ii) prior information from flow directions for cluster pair matching. Each matched cluster pair is considered to be generated by the edges of the same potential grid circle, and would be used to estimate time-varying ellipses. Finally, ellipse centers would be organized as an ordered grid pattern. For detailed methodology, please refer to the following sections.

### B. Event-Based Normal Flow Estimation

We first perform event-based normal flow estimation for subsequent event clustering and matching. Given the event stream in a time window of  $\Delta\tau$ , we accumulate raw events

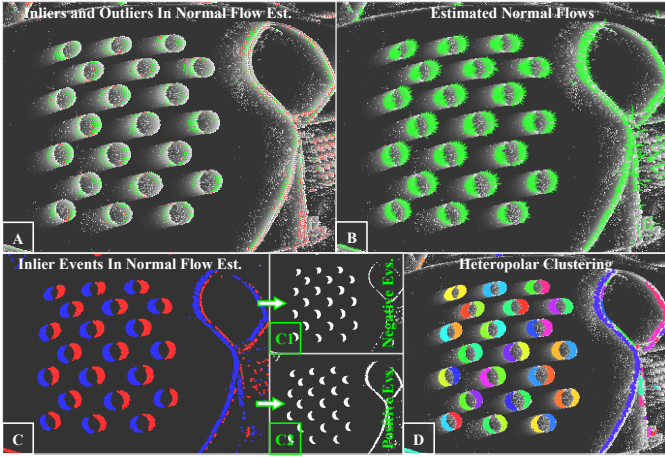


Fig. 3. Schematic of event clustering. Subfigure **A**: events with high (green) and low (red) inlier rates in the plane fitting. Subfigure **B**: the estimated normal flows (green lines). Subfigure **C**: inlier events, blue ones are positive events (**C2**) while red ones are negative events (**C1**). Subfigure **D**: clustering results, different colors represent distinct clusters.

$\mathcal{E} \triangleq \{e_j\}$  and subsequently construct the time surface map  $\mathcal{S}_{tm}$  and polarity surface map  $\mathcal{S}_{pol}$  using  $\mathcal{E}$ . The  $\mathcal{S}_{tm}$  and  $\mathcal{S}_{pol}$  record the timestamp and polarity of **the most recent** event at each pixel respectively, which support direct revisiting of the most recent raw event at a given pixel  $\mathbf{x}_k$  as follows:

$$\mathcal{E}_{srf} \triangleq \{e_k\}, e_k \leftarrow \{\mathcal{S}_{tm}(\mathbf{x}_k), \mathbf{x}_k, \mathcal{S}_{pol}(\mathbf{x}_k)\} \quad (9)$$

$$\text{s.t. } \mathcal{S}_{tm} \in \mathbb{R}^{w \times h}, \mathbf{x}_k \in \mathcal{I}, \mathcal{S}_{pol} \in \{-1, +1\}^{w \times h}$$

where  $w$  and  $h$  denote the width and height of vision sensor;  $\mathcal{E}_{srf}$  represents active event set lying on the surface. Subsequently, for each active event, we fit a spatiotemporal plane using its spatial neighboring active events (within a fixed-size window) based on the random sample consensus (RANSAC). The spatiotemporal plane is parameterized as follows:

$$[x \ y \ \tau \ 1] \cdot \mathbf{\Pi} = 0 \quad \text{s.t.} \quad \mathbf{\Pi} = [\Pi_a \ \Pi_b \ 1 \ \Pi_c]^\top \quad (10)$$

where  $\Pi_a$ ,  $\Pi_b$ , and  $\Pi_c$  are parameters of plane  $\mathbf{\Pi}$  to be determined. The normal flow of this event then can be obtained based on the fitted plane and (8) as follows:

$$\mathbf{n} = -\frac{1}{\Pi_a^2 + \Pi_b^2} \cdot \begin{bmatrix} \Pi_a \\ \Pi_b \end{bmatrix} \quad (11)$$

Note that an implicit assumption exists here that the brightness gradient direction is orthogonal to the edges [29]. Also, note that only those active events whose associated planes exhibit a high inlier rate in the RANSAC-based plane fitting are selected as inlier events for normal flow computation, see subfigures **{A}** and **{B}** in Fig. 3. For convenience, we denote the set of inlier events as:

$$\mathcal{E}_{inlier} \triangleq \{e_k | e_k \in \mathcal{E}_{srf}, r_k > r_{thd}\} \quad (12)$$

where  $r_k$  denotes the inlier rate of event  $e_k$  in the RANSAC-based spatiotemporal plane fitting. The corresponding normal flow set of  $\mathcal{E}_{inlier}$  is represented as  $\mathcal{N}$ .

### C. Spatiotemporal Ellipse Estimation

Subsequently, event clustering would be performed on obtained  $\mathcal{E}_{inlier}$ . The event clusters are then matched as one-to-one pairs for time-varying ellipse fitting.

1) *Homopolar Event Clustering*: Since  $\mathcal{E}_{inlier}$  lies on the surface of active events where no temporal overlap occurs, we conduct clustering in spatial domain, i.e., the 2D image plane,

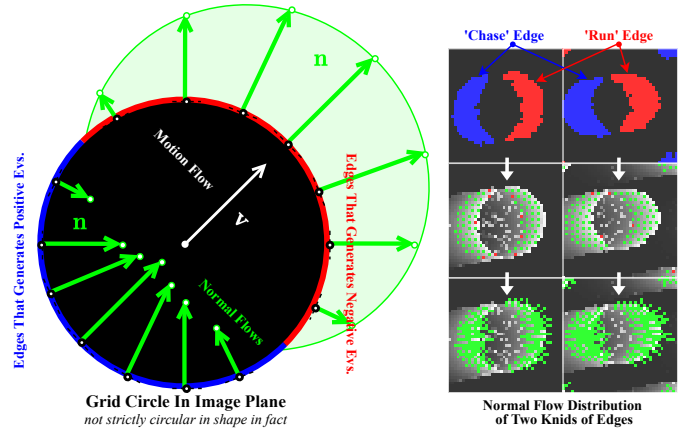


Fig. 4. Illustration of the normal flow distribution of edges of grid circles in the image plane. The relative motion between the circle and the camera results in two types of events generated by edges, which exhibit significant distinguishability regarding the directions of the normal flows.

for efficiency. Noting that the circle edges generally generate events of two polarities (see Fig. 4), we perform homopolar clustering, i.e., clustering independently for the events of each polarity, see subfigures **{C}**, **{C1}**, and **{C2}** in Fig. 3. To cluster events, the contour searching algorithm [30] is first employed to identify the contours of event clusters. Events within the same contour are then treated as a single cluster, see subfigure **{D}** in Fig. 3. We denote obtained clusters as:

$$\mathcal{C} \triangleq \{c^k | c^k \leftarrow (\mathcal{E}^k, \mathcal{N}^k)\} \quad \text{s.t.} \quad (13)$$

$$\mathcal{E}^k \simeq \mathcal{E}_{inlier}^k \triangleq \{e_j^k | e_j^k \in \mathcal{E}_{inlier}\}, \mathcal{N}^k \triangleq \{n_j^k | n_j^k \in \mathcal{N}\}.$$

Note that events within a cluster **share** the same polarity.

2) *Run-Chase Cluster Matching*: The relative motion between the circle grid and the camera, particularly the parallel shaking of the camera in front of grid circles, results in two event clusters with opposite polarities, see Fig. 4. Additionally, since the brightness gradient direction is almost orthogonal to the edges of grid circles, the normal flows of events in two clusters associated with a grid circle exhibit distinct distributions. We intuitively designate the two clusters associated with the same circle as the **running** cluster and the **chasing** cluster. Our objective is to identify running-chasing cluster pairs of potential grid circles for time-varying ellipse fitting.

We begin by assigning an initial label of *running*, *chasing*, or *unknown* to each cluster  $\mathcal{C}^k$ , based on the distribution of normal flow directions. The following indicator matrix is first computed for each cluster as the discriminant of cluster label:

$$\bar{\mathbf{L}}^k = \frac{\mathbf{L}_{avg}^k}{\|\mathbf{L}_{avg}^k\|}, \mathbf{L}_{avg}^k = \frac{1}{m} \sum_{j=0}^m \begin{bmatrix} l(d_j^k) \cdot l(s_j^k) & l(d_j^k) \cdot l(-s_j^k) \\ l(-d_j^k) \cdot l(s_j^k) & l(-d_j^k) \cdot l(-s_j^k) \end{bmatrix} \quad (14)$$

with

$$d_j^k = \mathbf{n}_j^k \times \bar{\mathbf{n}}^k, \quad s_j^k = (\mathbf{x}_j^k - \bar{\mathbf{x}}^k) \times \bar{\mathbf{n}}^k, \quad \bar{\mathbf{n}}^k = \frac{\mathbf{n}_{avg}^k}{\|\mathbf{n}_{avg}^k\|}, \quad (15)$$

$$\mathbf{n}_{avg}^k = \frac{1}{m} \sum_{j=0}^m \mathbf{n}_j^k, \quad \bar{\mathbf{x}}^k = \frac{1}{m} \sum_{j=0}^m \mathbf{x}_j^k, \quad l(z) \triangleq \begin{cases} 1, & z > 0, \\ 0, & z \leq 0 \end{cases}$$

where  $d_j^k$  and  $s_j^k$  are values that indicate the location of the normal flow  $\mathbf{n}_j^k$  and position  $\mathbf{x}_j^k$  of an event  $e_j^k$  respectively, relative to the average normal flow  $\bar{\mathbf{n}}^k$  and position  $\bar{\mathbf{x}}^k$ . For the ideal cases of running, chasing, and other (unknown) clusters,

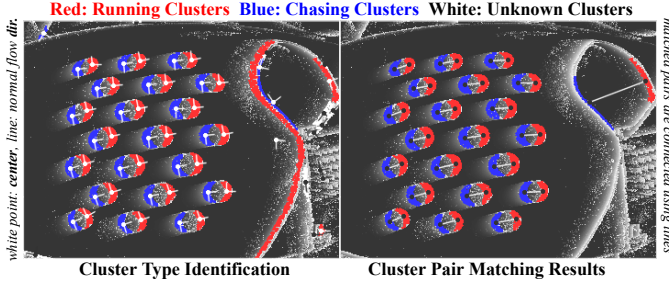


Fig. 5. Schematic of cluster type identification (left) and matching (right).

**Algorithm 1** First-Stage Run-Chase Cluster Matching

- 1: **Input:** event clusters  $\mathcal{C}$  and corresponding (inlier) raw events  $\mathcal{E}$ , normal flows  $\mathcal{N}$ , and labels  $\mathcal{L}$ .
- 2: **Output:** One-to-one cluster pairs  $\mathcal{P}$ .
- 3: **for** each cluster  $\mathcal{C}^i \in \mathcal{C}$  labeled as  $\mathcal{L}_{\text{chase}}$  **do**
- 4:   Initialize candidate cluster  $\mathcal{C}^k$ , distance  $d^{ik}$ , index  $k$ .
- 5:   **for** each cluster  $\mathcal{C}^j \in \mathcal{C}$  labeled as  $\mathcal{L}_{\text{run}}$  **do**
- 6:     Compute cluster distance  $d^{ij}$  using (18).
- 7:     **if**  $d^{ij} < d^{ik}$  **then**
- 8:        $\mathcal{C}^k \leftarrow \mathcal{C}^j, d^{ik} \leftarrow d^{ij}, k \leftarrow j$ .
- 9:     **end if**
- 10:   **end for**
- 11:   Store the correspondence:  $\mathcal{P} \leftarrow (\mathcal{C}^i, \mathcal{C}^k, d^{ik})$ .
- 12: **end for**
- 13: Eliminate ambiguous pairs in  $\mathcal{P}$  (multiple chasing clusters may be matched to the same running cluster) using the proximity principle, i.e., using stored cluster distance  $d^{ik}$ .
- 14: **Note:** The cluster pair distance  $d^{ij}$  is defined as:
 
$$d^{ij} \triangleq \text{Distance}(\mathcal{C}^i, \mathcal{C}^j) = \|\bar{\mathbf{x}}^{ij}\| \quad \text{s.t.} \quad \bar{\mathbf{x}}^{ij} \triangleq \bar{\mathbf{x}}^i - \bar{\mathbf{x}}^j. \quad (18)$$

If two clusters have different polarities ( $p^i \neq p^j$ ), large difference for normal flow directions ( $\bar{\mathbf{n}}^i \cdot \bar{\mathbf{n}}^j < \theta_{\text{thd}}$ ), or large misalignment ( $\bar{\mathbf{x}}^i \cdot \bar{\mathbf{n}}^{ij} < \theta_{\text{thd}}$ ), their distance  $d^{ij}$  would be set to infinity.

the indicator matrices have the following forms:

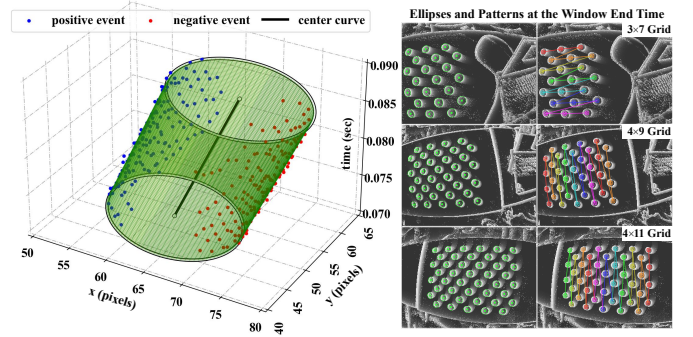
$$\bar{\mathbf{L}}_{\text{run}} = \begin{bmatrix} \sqrt{2}/2 & 0 \\ 0 & \sqrt{2}/2 \end{bmatrix}, \bar{\mathbf{L}}_{\text{chase}} = \begin{bmatrix} 0 & \sqrt{2}/2 \\ \sqrt{2}/2 & 0 \end{bmatrix}, \bar{\mathbf{L}}_{\text{unk}} = \begin{bmatrix} 1/2 & 1/2 \\ 1/2 & 1/2 \end{bmatrix} \quad (16)$$

Based on this fact, we perform the Frobenius norm-based similarity metric for each cluster using indicator matrices, and ultimately determine the unique label of each cluster:

$$\text{Similarity}(\bar{\mathbf{L}}^k, \bar{\mathbf{L}}_{(\cdot)}) \triangleq 1 - \frac{\|\bar{\mathbf{L}}^k - \bar{\mathbf{L}}_{(\cdot)}\|_F}{\|\bar{\mathbf{L}}_{(\cdot)}\|_F}, \|\mathbf{A}\|_F \triangleq \sqrt{\sum_{i,j} |a_{ij}|^2} \quad (17)$$

where  $\|\mathbf{A}\|_F$  denotes the Frobenius norm of matrix  $\mathbf{A}$ . The label of  $\mathcal{C}^k$ , denoted as  $\mathcal{L}^k$ , would be determined as  $\mathcal{L}_{\text{run}}$ ,  $\mathcal{L}_{\text{chase}}$ , or  $\mathcal{L}_{\text{unk}}$  based on the principle of maximum similarity.

Finally, we perform three-stage cluster pair matching, aiming to thoroughly search for potential matching pairs: (i) *running-chasing matching*: matching between clusters labeled as  $\mathcal{L}_{\text{run}}$  and  $\mathcal{L}_{\text{chase}}$ ; (ii) *running/chasing-unknown matching*: matching unmatched  $\mathcal{L}_{\text{run}}$  or  $\mathcal{L}_{\text{chase}}$  clusters with  $\mathcal{L}_{\text{unk}}$  clusters; (iii) *unknown-unknown matching*: matching among unmatched  $\mathcal{L}_{\text{unk}}$  clusters. To enhance readers' understanding, the **first-stage** matching process is summarized in Algorithm 1, while cluster matching results are shown in Fig. 5.

Fig. 6. Schematic of time-varying ellipse fitting. The linear time-varying ellipse  $E$  (see left subfigure) derived from raw events would be temporally sampled to organize grid patterns (see right subfigures).

3) *Time-Varying Ellipse Fitting*: After event clustering and cluster pair matching, raw events corresponding to potential grid circles are grouped for subsequent time-varying ellipse fitting. Note that our preceding operations (such as clustering and matching) involve only filtering and classification of raw events, thus the **original** sensor measuring information (raw events) is preserved.

Due to the oblique perspective and imaging distortions, the projection of a 3D circle onto the 2D image plane often results in a shape that no longer maintains its circular form (also not regular ellipses). We approximate it using the ellipse for simplicity. As a result, each raw event in a cluster pair lies on the edges of a 2D ellipse that is temporally synchronized with the event. We utilize a linear time-varying ellipse  $E$  to model all events within a cluster pair, which is parameterized as:

$$E(c_{x|y}(\tau), \lambda_{x|y}(\tau), \alpha) : \frac{(x' - c_x(\tau))^2}{(\lambda_x(\tau))^2} + \frac{(y' - c_y(\tau))^2}{(\lambda_y(\tau))^2} = 1 \quad (19)$$

with

$$\mathbf{x}' = \mathbf{R}(\alpha) \cdot \mathbf{x} \quad \text{s.t.} \quad \mathbf{x} = [x \ y]^\top, \mathbf{x}' = [x' \ y']^\top \quad (20)$$

where  $\mathbf{R}(\alpha) \in \text{SO}(2)$  denotes the time-invariant rotation of  $E$ ;  $c_{x|y}(\tau) \in P_1$  and  $\lambda_{x|y}(\tau) \in P_1$  represent the time-varying center and axes of  $E$  respectively, all of them are first-degree polynomials in time  $\tau$ , i.e.,  $P_1(\tau) = a_0 \cdot \tau + a_1$ . Time-varying ellipse fitting is to determine coefficients of polynomial  $c_{x|y}(\tau)$  and  $\lambda_{x|y}(\tau)$ , and the rotation angle  $\alpha$ . Specifically, for the  $i$ -th cluster pair  $\mathcal{P}^i$ , its associated  $E^i$  can be estimated by solving the following nonlinear least-squares problem:

$$\hat{E}^i \leftarrow \arg \min_{\tau} \sum_{j=0}^m \|r(\hat{\mathbf{e}}_j^i)\|^2 \quad (21)$$

with

$$r(\hat{\mathbf{e}}_j^i) \triangleq \hat{\lambda}_y^2(\tau)(\hat{x}' - \hat{c}_x(\tau))^2 - \hat{\lambda}_x^2(\tau)(\hat{y}' - \hat{c}_y(\tau))^2 - \hat{\lambda}_x^2(\tau)\hat{\lambda}_y^2(\tau) \quad (22)$$

where  $r(\hat{\mathbf{e}}_j^i)$  denotes the residual of event  $\mathbf{e}_j^i$ . The problem described in (21) would be solved in *Ceres* [31]. Once  $E^i$  is determined, the ellipse at a specific timestamp  $\tau$ , denoted as  $E^i(\tau)$ , can be obtained through temporally sampling time-varying  $c_{x|y}(\tau)$ ,  $\lambda_{x|y}(\tau)$ , and rotation angle  $\alpha$ , see Fig. 6.

**D. Visual Intrinsic Estimation**

Finally, we identify circle grid patterns from fitted ellipses, and perform visual intrinsic optimization to obtain final intrinsics. Specifically, for the  $k$ -th time window  $[\tau_s^k, \tau_e^k)$ , we perform normal flow estimation, event clustering, cluster pair matching, and time-varying ellipse fitting using in-window raw

events. All fitted time-varying ellipses would be temporally sampled at time point  $\tau_e^k$  to obtain synchronous 2D ellipses  $\{E^i(\tau_e^k)\}$ . **Centers** of 2D ellipses then would be organized as grid pattern using interface `findCirclesGrid(\cdot)` in *OpenCV* [32], see Fig. 6. The found **ordered** grid pattern in the  $k$ -th time window is represented as:

$$\mathcal{G}^k \triangleq \left\{ (\mathbf{x}_j^k, \mathbf{p}_j^w) \mid \mathbf{x}_j^k = [c_x^j(\tau_e^k), c_y^j(\tau_e^k)]^\top \in \mathbb{R}^2, \mathbf{p}_j^w \in \mathbb{R}^3 \right\} \quad (23)$$

where  $\mathbf{x}_j^k$  denotes the 2D projection of the 3D center point of the  $j$ -th grid circle (i.e., the  $\mathbf{p}_j^w$  parameterized in  $\mathcal{F}_{\rightarrow w}$ ).

To accurately recover camera intrinsics, we first randomly sample several grid patterns from  $\{\mathcal{G}^k\}$  and compute intrinsic guesses using `calibrateCamera(\cdot)` in *OpenCV*. The guesses with the lowest root-mean-square error (RMSE) would be selected as initials of intrinsics. Subsequently, based on intrinsic initials, PnP [33] is utilized to estimate camera poses  $\{\mathbf{T}_w^{c_k}\}$  associated with extracted grid patterns. Finally, a non-linear least-squares batch optimization (bundle adjustment) would be performed to refine all initialized states to global optimal ones, which can be expressed as follows:

$$\hat{\mathbf{x}}_{\text{intr}}, \{\hat{\mathbf{T}}_w^{c_k}\} \leftarrow \arg \min \sum_{k=0}^m \sum_{j=0}^{g_w \times g_h} \left\| \rho(\hat{\mathbf{x}}_j^k - \pi(\mathbf{p}_j^{c_k}, \hat{\mathbf{x}}_{\text{intr}})) \right\|^2 \quad (24)$$

with

$$\mathbf{p}_j^{c_k} = \hat{\mathbf{R}}_w \cdot \mathbf{p}_j^w + \hat{\mathbf{p}}_w^{c_k} \quad (25)$$

where  $\mathcal{F}_{\rightarrow c_k}$  is the camera frame associated with  $\mathcal{G}^k$ ;  $g_w$  and  $g_h$  represent the width (columns) and height (rows) of the grid;  $\rho(\cdot)$  denotes the Huber loss function [34];  $\pi(\cdot)$  is the visual projection function, which has been described in (3).

#### IV. REAL-WORLD EXPERIMENT

Extensive real-world experiments were conducted to validate the feasibility and effectiveness of the proposed method. This section presents the specific experiments and corresponding results.

##### A. Experimental Setup

The event camera, *DAVIS346*, with a resolution of  $346 \times 260$ , was employed in our experiments, which supports the acquisition of both raw event streams and conventional image frames. Asymmetric circle grid patterns in three different sizes ( $3 \times 7$ ,  $4 \times 9$ , and  $4 \times 11$ ) are utilized in our experiments (although *eKalibr* supports both symmetric and asymmetric patterns), see Fig. 7. The spacing and radius rate of three grid patterns are 50 mm and 2.5, respectively. For each pattern, we collected five data sequences, with each having a duration of 30 sec. The time window length for the event-based grid pattern recognition is configured to 0.02 sec.

##### B. Evaluation and Comparison of Calibration Performance

The calibration performance of *eKalibr* was first evaluated. To ensure the reliability and comprehensiveness of the evaluation, we selected three state-of-the-art and publicly available calibration methods for comparison with *eKalibr*:

- 1) **Frame-Based (DV [35]):** The calibration toolkit provided by the manufacturer of *DAVIS346* (i.e., *iniVation*).

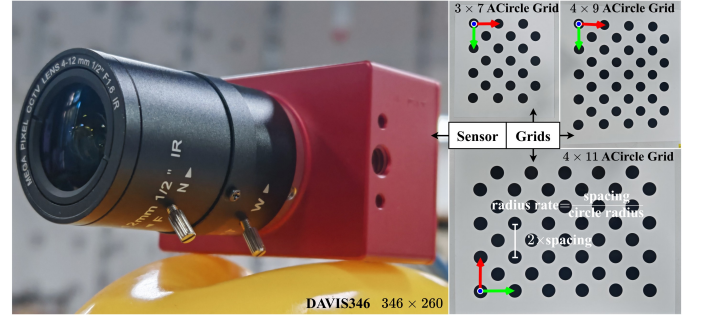


Fig. 7. Environmental setup about the equipment (left subfigure) and the circle grid patterns (right subfigures) utilized in real-world experiments.

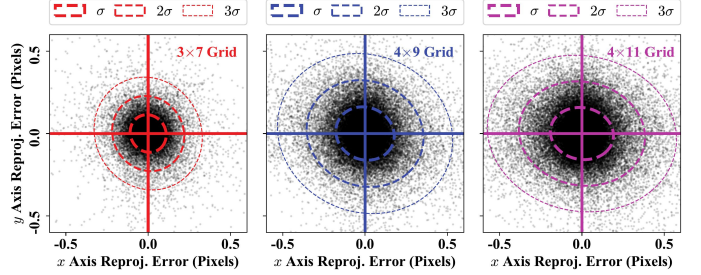


Fig. 8. The distribution of reprojection errors in *eKalibr* calibration on three different grids. Solid straight lines represent means of reprojection errors.

Since it's frame-based, the corresponding calibration results can be considered as the ground truth.

- 2) **E2VID [17] + Kalibr [5]:** The method described in [16], which utilizes *E2VID* [17] to reconstruct images from raw events, and then employs a frame-based calibration toolkit for intrinsic calibration (we use *Kalibr* [5] in our experiments, as [16] did).
- 3) **E-Calib [20]:** An event-only intrinsic calibration toolkit using asymmetric circles pattern. The circle grid extraction in *E-Calib* [20] is based on density-based spatial clustering (DBSCAN).

Table I summarizes the calibration results of four methods on grid patterns of three different sizes, where the mean and standard deviation (STD) of calibration results from Monte-Carlo experiments are provided. As can be seen, among the four methods, the conventional frame-based method achieved the best repeatability (smallest STD) with the lowest reprojection error. Among the other three event-only methods, *eKalibr* yielded results closest to those of frame-based method in terms of the mean, while also demonstrating better repeatability (as indicated by the bolded values in Table I).

Table II summarizes the grid detection success rates of three event-based methods on three kinds of grids. *E-Calib* directly employs DBSCAN clustering method for circle-edge-associated event identification, which exhibits a high dependency on parameters and is sensitive to noise. In contrast, *eKalibr* utilizes the normal flow estimation to identify inlier events, after which only simple clustering is sufficient to obtain high-quality circle-edge-associated events. As can be seen in Table II, *eKalibr* exhibits a higher detection success rate compared to *E2VID* and *E-Calib*.

TABLE I  
EVALUATION AND COMPARISON OF INTRINSIC CALIBRATION RESULTS IN REAL-WORLD MONTE-CARLO EXPERIMENTS  
EKALIBR ACHIEVES COMPARABLE RESULTS TO CONVENTIONAL FRAME-BASED CALIBRATION METHOD

Parameter	Frame-Based (DV [35])	E2VID [17] + Kalibr [5]	E-Calib [20]	eKalibr (Ours)	
3×7 ACircle Grid	$f_{x y}$	256.47±1.22, 256.39±1.25	246.59±6.78, 247.44±5.10	255.21±1.82, 254.09±1.86	255.30± <b>1.51</b> , 255.17± <b>1.52</b>
	$c_{x y}$	169.90±0.43, 122.17±0.09	167.36±1.29, 120.04±1.12	171.02±0.58, 121.33±0.40	170.03± <b>0.29</b> , 121.96± <b>0.31</b>
3×7 ACircle Grid	$k_1$	$-4.31e^{-1}±5.47e^{-3}$	$-3.80e^{-1}±1.38e^{-2}$	$-4.09e^{-1}±5.26e^{-3}$	$-4.27e^{-1}±$ <b><math>4.97e^{-3}</math></b>
	$k_2$	$2.84e^{-1}±1.86e^{-2}$	$3.21e^{-1}±5.34e^{-2}$	$2.68e^{-1}±$ <b><math>1.03e^{-2}</math></b>	$2.71e^{-1}±1.14e^{-2}$
	$p_1$	$7.56e^{-4}±4.37e^{-4}$	$9.00e^{-4}±1.49e^{-3}$	$3.97e^{-4}±6.82e^{-4}$	$1.85e^{-4}±$ <b><math>5.55e^{-4}</math></b>
	$p_2$	$-1.24e^{-2}±2.30e^{-2}$	$8.65e^{-2}±2.47e^{-1}$	$5.06e^{-4}±7.01e^{-4}$	$6.19e^{-4}±$ <b><math>2.86e^{-4}</math></b>
$\sigma_{proj}$	0.07	0.35	0.21	<b>0.11</b>	
4×9 ACircle Grid	$f_{x y}$	255.41±1.76, 255.43±1.77	249.72±5.05, 248.52±5.92	255.06± <b>0.98</b> , 256.89±1.22	254.57±1.05, 254.72± <b>1.02</b>
	$c_{x y}$	170.21±0.19, 123.64±0.34	169.02±1.04, 121.31±1.00	173.69±0.41, 123.61±0.34	169.44± <b>0.20</b> , 122.29± <b>0.17</b>
4×9 ACircle Grid	$k_1$	$-4.18e^{-1}±7.02e^{-3}$	$-3.97e^{-1}±9.97e^{-3}$	$-4.29e^{-1}±6.22e^{-3}$	$-4.21e^{-1}±$ <b><math>4.40e^{-3}</math></b>
	$k_2$	$2.54e^{-1}±1.35e^{-2}$	$3.03e^{-1}±5.47e^{-2}$	$2.68e^{-1}±$ <b><math>6.14e^{-3}</math></b>	$2.52e^{-1}±7.79e^{-3}$
	$p_1$	$2.38e^{-4}±1.22e^{-4}$	$7.32e^{-4}±1.28e^{-3}$	$7.93e^{-4}±5.30e^{-4}$	$-4.44e^{-4}±$ <b><math>2.14e^{-4}</math></b>
	$p_2$	$-9.38e^{-2}±1.10e^{-2}$	$-1.65e^{-3}±1.21e^{-1}$	$3.63e^{-4}±3.39e^{-4}$	$8.81e^{-4}±$ <b><math>2.82e^{-4}</math></b>
$\sigma_{proj}$	0.06	0.37	0.28	<b>0.17</b>	
4×11 ACircle Grid	$f_{x y}$	255.91±0.42, 255.87±0.43	249.08±4.97, 251.20±4.70	255.73±1.03, 255.87± <b>0.91</b>	255.98± <b>0.98</b> , 256.10±1.00
	$c_{x y}$	170.01±0.20, 121.73±0.30	169.63±0.88, 121.41±0.56	171.02±0.63, 122.80±0.32	169.85± <b>0.23</b> , 121.73± <b>0.14</b>
4×11 ACircle Grid	$k_1$	$-4.23e^{-1}±2.02e^{-3}$	$-4.09e^{-1}±6.04e^{-3}$	$-4.24e^{-1}±4.36e^{-3}$	$-4.23e^{-1}±$ <b><math>3.77e^{-3}</math></b>
	$k_2$	$2.70e^{-1}±4.87e^{-3}$	$2.91e^{-1}±1.08e^{-2}$	$2.50e^{-1}±7.89e^{-3}$	$2.54e^{-1}±$ <b><math>6.50e^{-3}</math></b>
	$p_1$	$5.95e^{-4}±1.65e^{-4}$	$7.79e^{-4}±2.83e^{-4}$	$9.05e^{-4}±1.83e^{-4}$	$8.29e^{-4}±$ <b><math>1.62e^{-4}</math></b>
	$p_2$	$6.09e^{-4}±4.31e^{-4}$	$3.84e^{-4}±5.67e^{-3}$	$6.82e^{-4}±2.76e^{-4}$	$6.33e^{-4}±$ <b><math>2.64e^{-4}</math></b>
$\sigma_{proj}$	0.08	0.41	0.29	<b>0.21</b>	

\* The quantities presented in the row for  $f_{x|y}$  (pixels) are arranged in the order of  $f_x$  and  $f_y$ . This same ordering applies to  $c_{x|y}$  (pixels).

\* The value in each table cell is represented as (Mean) ± (STD). The item with the minimum STD in a row is highlighted in bold. The results in the column **Frame-Based (DV [35])** are considered as ground truth and are excluded from comparison when determining the minimum STD.

\*  $\sigma_{proj}$  denotes the root-mean-square (RMS) reprojection error in intrinsic calibration, unit: pixels.

TABLE II  
EVALUATION AND COMPARISON OF CIRCLE GRID EXTRACTION  
EKALIBR ACHIEVES THE HIGHEST DETECTION SUCCESS RATE

Method	3×7 Grid	4×9 Grid	4×11 Grid
E2VID [17]	43.180 %	37.898 %	52.617 %
E-Calib [20]	59.429 %	68.935 %	70.562 %
eKalibr (Ours)	76.933 %	80.520 %	74.280 %

\* The detection success rate is obtained by: the number of successful detections divided by the total number of detections.

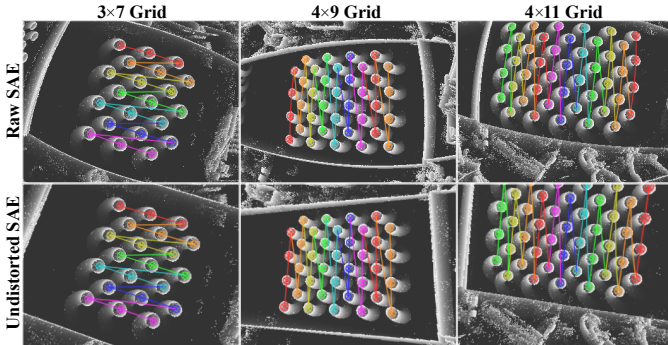


Fig. 9. Raw (distorted) SAE maps (top row) and undistorted ones (bottom row) based on intrinsics calibrated by *eKalibr*.

### C. Consistency Evaluation

The corresponding distributions of reprojection errors for the RMS values presented in Table I are illustrated in Fig. 8 for further evaluation of calibration consistency. It can be seen that the reprojection errors approximately follow a zero-mean normal distribution. Among the three grid patterns, the reprojection error distribution corresponding to the 3×7 grid

TABLE III  
COMPUTATION CONSUMPTION IN EKALIBR  
GRID EXTRACTION CONSUMED THE MAJORITY OF THE PROCESSING TIME

Config.	OS Name	Ubuntu 20.04.6 LTS 64-Bit	
	Processor	12th Gen Intel® Core™ i9	
		Graphics	
		Mesa Intel® Graphics	
Scenes	Computation Consumption (unit: minute)		
	Grid Extraction	Intrinsic Est.	Total
3×7 Grid	1.402	0.047	1.449
4×9 Grid	2.078	0.103	2.181
4×11 Grid	2.350	0.105	2.455

\* The reported time represents the average time consumption across multiple (five) runs, with each data sequence lasting 30 seconds.

is the most concentrated, exhibiting the smallest variance. Fig. 9 illustrates the SAE maps before and after distortion correction using the intrinsics estimated by *eKalibr*. It can be found that the structures in undistorted images align well with their counterparts in the real world, demonstrating a high consistency.

### D. Computation Consumption Evaluation

Table III summarizes the computational time consumption of *eKalibr* in real-world experiments. It can be seen that for a 30-second-long dataset, the average time consumption of *eKalibr* is approximately two minutes, with the majority of the time spent on grid extraction. As the grid size increases, the time consumption reasonably grows.

## V. CONCLUSION

In this article, we present an open-sourced visual intrinsic calibration method for event cameras, named *eKalibr*, which extracts accurate patterns from raw events generated by a

circle grid board for intrinsic determination. Specifically, We first perform event-based normal flow estimation to filter out potential events generated by circle edges. The filtered events are then clustered in the spatial domain to obtain event clusters for circle-oriented one-to-one matching. Each matched cluster pair is regarded as corresponding to the same potential grid circle, and would be utilized for time-varying ellipse estimation. Finally, temporally synchronized grid patterns would be extracted from ellipse centers for final visual intrinsic calibration. We conduct sufficient experiments to evaluate the proposed *eKalibr*, and the results demonstrate that *eKalibr* is capable of accurate grid pattern extraction and intrinsic calibration. In future work, we will support multi-camera and event-inertial spatiotemporal calibration in *eKalibr*.

#### ACKNOWLEDGMENTS

Suolong Chen would like to express his gratitude to the School of Geodesy and Geomatics, Wuhan University, and the GREAT team for providing experimental equipment.

#### CREDIT AUTHORSHIP CONTRIBUTION STATEMENT

**Suolong Chen:** Conceptualisation, Methodology, Software, Validation, Original Draft. **Xingxing Li:** Supervision, Funding Acquisition, Review and Editing. **Liu Yuan and Ziao Liu:** Data Curation, Review and Editing.

#### REFERENCES

- [1] G. Gallego, T. Delbrück, G. Orchard, C. Bartolozzi, B. Taba, A. Censi, S. Leutenegger, A. J. Davison, J. Conradt, K. Daniilidis *et al.*, “Event-based vision: A survey,” *IEEE transactions on pattern analysis and machine intelligence*, vol. 44, no. 1, pp. 154–180, 2020.
- [2] K. Huang, S. Zhang, J. Zhang, and D. Tao, “Event-based simultaneous localization and mapping: A comprehensive survey,” *arXiv preprint arXiv:2304.09793*, 2023.
- [3] C. Brandli, R. Berner, M. Yang, S.-C. Liu, and T. Delbruck, “A 240×180 130 db 3 μs latency global shutter spatiotemporal vision sensor,” *IEEE Journal of Solid-State Circuits*, vol. 49, no. 10, pp. 2333–2341, 2014.
- [4] S. Chen and M. Guo, “Live demonstration: Celex-v: A 1m pixel multi-mode event-based sensor,” in *2019 IEEE/CVF Conference on Computer Vision and Pattern Recognition Workshops (CVPRW)*. IEEE, 2019, pp. 1682–1683.
- [5] E. Z. A. S. Lab, “Kalibr: visual-inertial calibration toolbox,” <https://github.com/ethz-asl/kalibr>, accessed: 2024-12-29.
- [6] Y. Suh, S. Choi, M. Ito, J. Kim, Y. Lee, J. Seo, H. Jung, D.-H. Yeo, S. Namgung, J. Bong *et al.*, “A 1280×960 dynamic vision sensor with a 4.95-μm pixel pitch and motion artifact minimization,” in *2020 IEEE international symposium on circuits and systems (ISCAS)*. IEEE, 2020, pp. 1–5.
- [7] E. Olson, “Apriltag: A robust and flexible visual fiducial system,” in *2011 IEEE international conference on robotics and automation*. IEEE, 2011, pp. 3400–3407.
- [8] A. De la Escalera and J. M. Armingol, “Automatic chessboard detection for intrinsic and extrinsic camera parameter calibration,” *Sensors*, vol. 10, no. 3, pp. 2027–2044, 2010.
- [9] J. Wang and E. Olson, “Apriltag 2: Efficient and robust fiducial detection,” in *2016 IEEE/RSJ International Conference on Intelligent Robots and Systems (IROS)*. IEEE, 2016, pp. 4193–4198.
- [10] Z. Zhang, “A flexible new technique for camera calibration,” *IEEE Transactions on pattern analysis and machine intelligence*, vol. 22, no. 11, pp. 1330–1334, 2000.
- [11] D. Gorchard, “Dvs calibration,” 2025, accessed: January 3, 2025. [Online]. Available: <https://github.com/gorchard/DVScalibration.git>
- [12] R. (Robotics and P. Group), “rpg\_dvs\_ros,” 2025, accessed: January 3, 2025. [Online]. Available: [https://github.com/uzh-rpg/rpg\\_dvs\\_ros.git](https://github.com/uzh-rpg/rpg_dvs_ros.git)
- [13] B. Cai, A. Zi, J. Yang, G. Li, Y. Zhang, Q. Wu, C. Tong, W. Liu, and X. Chen, “Accurate event camera calibration with fourier transform,” *IEEE Transactions on Instrumentation and Measurement*, 2024.
- [14] S. Chen, X. Li, S. Li, Y. Zhou, and X. Yang, “ikalibr: Unified targetless spatiotemporal calibration for resilient integrated inertial systems,” *arXiv preprint arXiv:2407.11420*, 2024.
- [15] M. Gehrig, W. Aarents, D. Gehrig, and D. Scaramuzza, “Dsec: A stereo event camera dataset for driving scenarios,” *IEEE Robotics and Automation Letters*, vol. 6, no. 3, pp. 4947–4954, 2021.
- [16] M. Muglikar, M. Gehrig, D. Gehrig, and D. Scaramuzza, “How to calibrate your event camera,” in *Proceedings of the IEEE/CVF conference on computer vision and pattern recognition*, 2021, pp. 1403–1409.
- [17] H. Rebecq, R. Ranftl, V. Koltun, and D. Scaramuzza, “High speed and high dynamic range video with an event camera,” *IEEE transactions on pattern analysis and machine intelligence*, vol. 43, no. 6, pp. 1964–1980, 2019.
- [18] L. Zhu, X. Wang, Y. Chang, J. Li, T. Huang, and Y. Tian, “Event-based video reconstruction via potential-assisted spiking neural network,” in *Proceedings of the IEEE/CVF Conference on Computer Vision and Pattern Recognition*, 2022, pp. 3594–3604.
- [19] K. Huang, Y. Wang, and L. Kneip, “Dynamic event camera calibration,” in *2021 IEEE/RSJ International Conference on Intelligent Robots and Systems (IROS)*. IEEE, 2021, pp. 7021–7028.
- [20] M. Salah, A. Ayyad, M. Humais, D. Gehrig, A. Abusafieh, L. Seneviratne, D. Scaramuzza, and Y. Zweiri, “E-calib: A fast, robust and accurate calibration toolbox for event cameras,” *IEEE Transactions on Image Processing*, 2024.
- [21] S. Wang, Z. Xin, Y. Hu, D. Li, M. Zhu, and J. Yu, “Ef-calib: Spatiotemporal calibration of event-and frame-based cameras using continuous-time trajectories,” *arXiv preprint arXiv:2405.17278*, 2024.
- [22] J. Kannala and S. S. Brandt, “A generic camera model and calibration method for conventional, wide-angle, and fish-eye lenses,” *IEEE transactions on pattern analysis and machine intelligence*, vol. 28, no. 8, pp. 1335–1340, 2006.
- [23] V. Usenko, N. Demmel, and D. Cremers, “The double sphere camera model,” in *2018 International Conference on 3D Vision (3DV)*. IEEE, 2018, pp. 552–560.
- [24] Z. Tang, R. G. Von Gioi, P. Monasse, and J.-M. Morel, “A precision analysis of camera distortion models,” *IEEE Transactions on Image Processing*, vol. 26, no. 6, pp. 2694–2704, 2017.
- [25] G. Zhou, H. Li, R. Song, Q. Wang, J. Xu, and B. Song, “Orthorectification of fisheye image under equidistant projection model,” *Remote Sensing*, vol. 14, no. 17, p. 4175, 2022.
- [26] W. Xu, X. Peng, and L. Kneip, “Tight fusion of events and inertial measurements for direct velocity estimation,” *IEEE Transactions on Robotics*, 2023.
- [27] B. K. Horn and B. G. Schunck, “Determining optical flow,” *Artificial intelligence*, vol. 17, no. 1-3, pp. 185–203, 1981.
- [28] T. Delbruck *et al.*, “Frame-free dynamic digital vision,” in *Proceedings of Intl. Symp. on Secure-Life Electronics, Advanced Electronics for Quality Life and Society*, vol. 1. Citeseer, 2008, pp. 21–26.
- [29] X. Lu, Y. Zhou, J. Niu, S. Zhong, and S. Shen, “Event-based visual inertial velometer,” *arXiv preprint arXiv:2311.18189*, 2023.
- [30] S. Suzuki *et al.*, “Topological structural analysis of digitized binary images by border following,” *Computer vision, graphics, and image processing*, vol. 30, no. 1, pp. 32–46, 1985.
- [31] S. Agarwal, K. Mierle, and T. C. S. Team, “Ceres Solver,” 10 2023. [Online]. Available: <https://github.com/ceres-solver/ceres-solver>
- [32] G. Bradski, “The OpenCV Library,” *Dr. Dobb’s Journal of Software Tools*, 2000.
- [33] V. Lepetit, F. Moreno-Noguer, and P. Fua, “Epnnp: An accurate o(n) solution to the pnp problem,” *International journal of computer vision*, vol. 81, pp. 155–166, 2009.
- [34] P. J. Huber, “Robust estimation of a location parameter,” in *Breakthroughs in statistics: Methodology and distribution*. Springer, 1992, pp. 492–518.
- [35] Inivation, “Dv tool documentation,” <https://docs.inivation.com/software/dv/index.html>, accessed: 2024-12-30.